DESIGN AND PRELIMINARY STUDY OF A 200W CYLINDRICAL HALL THRUSTER

Tatiana Perrotin (1), Adrián Domínguez-Vázquez (1), Jaume Navarro-Cavallé (1), Pablo Fajardo (1), Eduardo Ahedo (1)

(1) Equipo de Propulsión Espacial y Plasmas, Universidad Carlos III de Madrid, Avenida de la Universidad, 30, 28911 Leganés (Spain), Email: tperroti@pa.uc3m.es

KEYWORDS:

cylindrical hall thruster, hybrid PIC/fluid plasma simulation, prototype design, micro-propulsion, low-power thruster

ABSTRACT:

Multiple simulations of a Cylindrical Hall Thruster (CHT) are performed using the hybrid PIC/fluid plasma code HYPHEN. This numerical research attempts to explore the effect of isolated (important) parameters. The design of a test prototype is introduced for a future comparison of experimental and computational results.

1. INTRODUCTION

Low-power propulsion systems have aroused great interest in the last years since they enable the use of lighter satellites and constellations with reduced costs, but they require development since existing legacy on low power thrusters is limited. A problem that arises when downscaling electric thrusters is the high surface-to-volume ratio [1]; the efficiency and the thruster lifetime decrease as a consequence of the increase of power losses, erosion and temperature. Besides, the reduction of the size of the components is a challenge for manufacturing and structural integrity. A way to reduce wall losses in a Hall Effect Thruster (HET) is to remove the central core, partially or entirely. This cylindrical channel geometry has been studied experimentally and theoretically by several groups in the last two decades [2–6] but it still requires some optimization and understanding, specifically regarding some internal phenomena such as electron cross-field transport and plasma-wall interaction. Thus, this design option offers an innovative and challenging path, yet with some existing knowledge basis. The CHT introduced here is sized for a target power range of 100 to 300 W, with a simple design. The prototype is the first iteration and its plasma plume behaviour will be studied with common diagnostics. As a preliminary approach, a plasma numerical simulation study of the CHT is presented here, to understand the effect of various geometry and discharge parameters on the thruster operation such as the anode and injector position, the channel length, the cathode location and the effects of partial electron thermalization. A good comprehension of these effects shall provide guidelines for design improvements, while future experimental studies of the prototype are expected to help to validate the HYPHEN simulation tool [7]. The design of the CHT to be used for those tests is first described synthetically and then the simulation results are presented.

2. EXPERIMENTAL STUDY OF CHT

2.1. Prototype design

A prototype has been designed for extensive experimental characterization in the future. This 100-300W thruster, represented in fig. 1 and fig. 2, is made of a 22 mm long, 13 mm radius, fully cylindrical channel (FCHT[1]). This geometry option is expected to further reduce erosion of the central magnetic pole by removing it entirely, thereby extending the thruster lifetime. It is also a simpler design to scale down compared to the only partially cylindrical HET, which makes the manufacturing of the components easier. Removing the annular part might result in a slight decrease in neutral density and thus in the propellant utilization, but an FCHT can still surpass the performance of a CHT as observed in [6].

The shape of the magnetic field of the designed thruster is displayed in fig. 3 (radial and axial components along axis and sidewall are also shown in fig. 9L$_3$, these figures actually shows the field used in the simulations, the one used in the prototype has the same shape but a slightly weaker flux). It was chosen to be similar to some FCHT presented in the literature [4,6,8–10], specifically in some key locations: near the central pole, near the anode and near the sidewall at the exit plane. The field near the axis is around 1200G, much stronger than in the lens of conventional annular Hall thrusters, while it is around 100G near the exit. The field is globally stronger than in larger HET to ensure that electrons are magnetized, and ions are not. It is suggested that the resulting mirror topology plays

[1] FCHT is often referred to as CHT which includes both fully and partially cylindrical HET, in this document 'CHT' is used

an important role in trapping electrons [10]. This magnetic field is generated by two coils. This allows for tuning the magnetic field $\vec{B}$ to facilitate ignition or to study the effect of changing it, by varying the magnitude, sign and ratio of the currents in both coils. Electromagnets were also chosen because permanent magnets seem to induce a larger plume divergence angle [10] and easily lose their magnetic properties when the temperature rises. A direct field configuration, in which both coils are polarized in the same direction, will be used when firing the CHT since it affects positively the plume angle and generally enhances anode shielding [11,12].

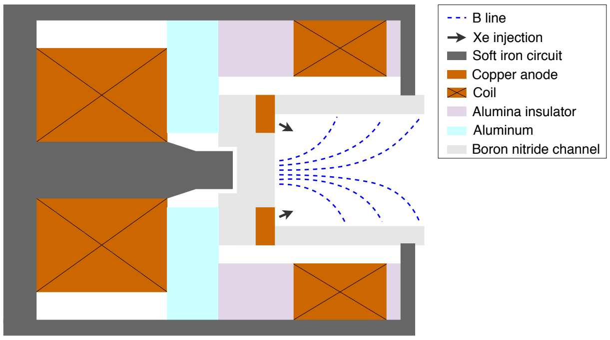

Figure 1: Schematic cross-section of the designed CHT showing the main components and the materials used (not to scale)

Good ionization is targeted by injecting the propellant through the anode, with multiple small holes evenly spread for azimuthal homogeneity of the neutral density in the channel. This electrode has an annular shape and its surface exposed to plasma is small to limit the electron collection area and is located on the back wall, at the outermost radius, where it benefits from the best shielding by the magnetic field.

Regarding the materials, boron nitride was selected for the channel walls due to its high operating temperature, low electrical conductivity even at high temperature, low thermal conductivity and expansion, and secondary electron emission properties. Alumina is chosen for structural parts that are not exposed to plasma and play a role in thermal and electrical insulation. Instead, aluminium and copper are used to avoid overheating of the anode that is exposed to large heat loads and of the enamel of the front coil. The thermally conducting and insulating components are arranged to create a heat dissipation path towards the thruster support to protect the critical elements that are limited in operating temperature. Eventually, the magnetic circuit is composed of pure iron for its very good magnetic permeability that remains unaltered at the expected operating temperatures. All the dimensions of the iron casing and core have been optimized to get the largest magnetic field for the nominal coils' currents.

2.2. Primary tests

Prior to ignition test, the thruster's magnetic field was measured at nominal current flowing in both coils and compared to the target magnetic field. The real field appeared to match relatively well the objective with a maximum discrepancy of 12%, although a slight misalignment of the coils induced minor asymmetry in the field. Then, several tests were performed to characterize the repeatability and the minimum conditions for ignition in terms of anode and cathode propellant flow rate, anode applied voltage, magnetic field and cathode keeper voltage and current. Ignition was obtained successfully with both the anode and the cathode running on xenon (fig. 2), as well as on krypton. However, stable operation with voltage control of the anode was not always reached. This is attributed to the use of an oversized cathode that requires a large discharge current to be self-heated. As a consequence, the cathode mass flow rate could not be reduced sufficiently and drawing current to the keeper electrode did not allow for optimal operation either. Besides, some asymmetric material deposition patterns were observed in the channel and were likely related to cathode effects. The use of a hot filament or a hollow cathode adapted to low currents is intended for future work, to determine the operating range of the CHT and perform measurements in the plasma plume.

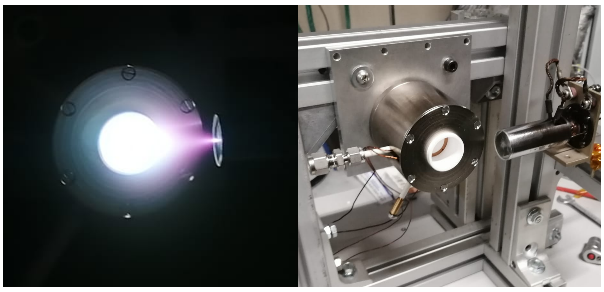

Figure 2: Thruster and hollow cathode firing on xenon (left) and thruster and cathode assembly (right)

So far, the thruster has shown the most satisfying behaviour with the settings $V_A = 200\,\mathrm{V}$, $\dot{m}_A = 0.3\,\mathrm{mg \cdot s^{-1}}$ (Xe) and a keeper current $I_k = 0.5\,\mathrm{A}$, which allowed the plasma to settle at a discharge current $I_d \approx 0.7\,\mathrm{A}$ but with the extremely large cathode mass flow rate $\dot{m}_C = 1.5\,\mathrm{mg \cdot s^{-1}}$. What appears to be the main consequence of $\dot{m}_C$ being too high is the large discharge current, thruster heating and difficulty to get a steady discharge. More experiments will be performed with this prototype, but the CHT operation has already been studied numerically and some results are presented hereafter.

3. NUMERICAL STUDY OF CHT

3.1. Review of existing works

Multiple research groups developed new numerical models or used existing ones to understand the specificities of CHT operation. Most of them considered Princeton's 2.6cm CHT operating around 100W for benchmarking, comparing computations and experimental results.

A quasi-1D model developed in 2003 by Smirnov [13] used fluid equations for all species. The geometry was the one of a HET with 'long walls', representing the transition region between annular and cylindrical parts of the CHT, where the magnetic field is the strongest and most of the potential drop is located[2]. The wall losses were then artificially reduced in the cylindrical part to account for the removed central wall. However, decreasing wall losses this way was insufficient to obtain a propellant utilization as good as observed experimentally [2,3], since electron-wall interaction seemed to limit the electron temperature and consequent ionization. Later on, a 2D axisymmetric hybrid code was developed by Garrigues [14] using particle-in-cell (PIC) representation of heavy particles and fluid equations for the electrons. It included anomalous Bohm-type cross-field transport in the electron momentum with a Bohm coefficient determined by fitting experimental results, and a parametric energy loss coefficient. Although good qualitative results were obtained, the authors mentioned some discrepancies with measurements of the plasma potential and density, which they attributed to the electron fluid model. A 3D PIC code was used by Matyash [15] to point out the existence, in the vicinity of the anode of Princeton's CHT, of an azimuthal rotating spoke affecting the neutral and plasma densities as well as the plasma potential and carrying a large portion of the electron cross-field current, therefore contributing to transport. Recently, a multiscale approach was adopted by Brieda [16] to simulate the same thruster, determining electron mobility along magnetic field lines with a 1D parallel kinetic code, and using it as an input for a 2D axial-radial code of the whole discharge that extends to a 3D code for the plume region. An improvement was observed in the agreement between computed and measured potential profiles. Eventually, Jiang [8] presented results of a full PIC code checked with the same 2.6cm CHT and later used with another CHT geometry to study some effects of the magnetic topology with shunts, providing interesting insight on optimization of the magnetic mirror ratio between the sidewall and the back wall.

3.2. Simulation environment

The code used to generate the simulations presented hereafter is adapted for multiple kinds of thrusters and is a modular hybrid 2D-axisymmetric code [7]. The heavy species, i.e. neutral atoms and ions are modelled with a PIC module in a structured, non-uniform mesh, in which particle injection, collisions and propagation are performed to obtain the production, densities and fluxes of those particles. The electrons are modelled as a fluid in a Magnetic Field Aligned Mesh (MFAM). Between two PIC steps, the electron fluid module and the auxiliary sheath module iterate, and the results are interpolated between the two meshes. The electric potential Φ and electron fluid properties (temperature T_e, current density vector j_e, heat flux vector q_e) are obtained after heavy particles are moved, by applying quasi-neutrality and solving for the current continuity and electron momentum, energy and heat flux equations. This set of equations incorporates the parameters α_{tm}, α_{te} and α_{tq} to account for turbulent cross-field transport for momentum, energy and heat flux, respectively [7].

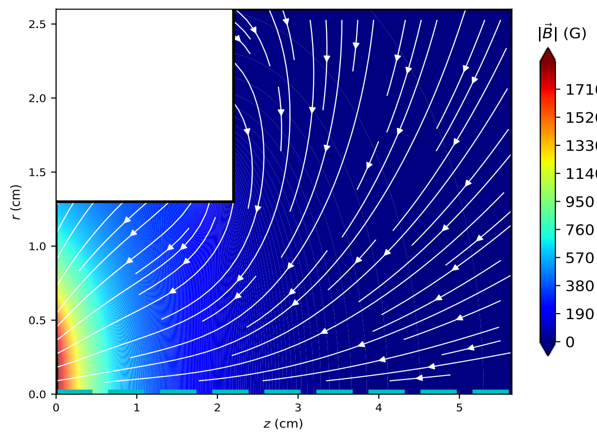

Figure 3: Magnetic flux and streamlines in the simulated CHT (dashed cyan line: axis of symmetry).

Fig. 3 displays the magnetic topology used in the following simulations of CHT. The typical domain used is displayed in fig. 4 and consists of an axis of symmetry, dielectric walls and free-loss plume boundaries, which are bound by a current-free condition. The thruster channel walls also contain a biased anode boundary drawing a net current, and an injection area for heavy particles. The chamber is fully cylindrical, which means that the anode and upstream wall are flush, and its dimensions are: 22 mm long, 13 mm radius. The wall sheath model includes true secondary electron emission (SEE),

[2] This is specific of the non-fully cylindrical Hall thruster

primary electron reflection, and a partial thermalization factor accounting for the replenishment of the electron velocity distribution function, with the possibility of adjusting properties of wall materials and propellant. Collisions in the plasma include single and multiple ionization of neutrals by electron impact, re-ionization of ion by electron impact, neutral excitation and finally elastic and Coulomb collisions according to existing models. The ‘volumetric cathode’ placed in the near plume is the source of electrons and is always used as the electric potential reference. The propellant injected in the domain is xenon and the thruster walls are all taken to be ceramic (boron-nitride). The anode is biased to 200V and an RLC filter is included in the discharge circuit to damp large oscillations of the discharge current (although, the results presented here have little oscillations independently of the use of the filter). The oscillation regime has been observed to be highly dependent on the chosen anomalous transport parameters, but this study will be developed in a future publication.

3.3. Parametric studies

3.3.1. Anode and injection location

In this section, the anode and neutral gas injection area is displaced as shown in fig. 4 to study the consequences. The radial width (for A_1 to A_4) of this annular surface is kept approximately constant and all the other parameters are identical for all six cases, except case A_1 in which the mass flow rate $\dot{m}_a$ was reduced to $0.6\ \mathrm{mg \cdot s^{-1}}$ to keep a low discharge power. Given the presence of small oscillations in the discharge current ($\Delta I_d < \overline{I_d}$), all mentioned or represented magnitudes are time-averages.

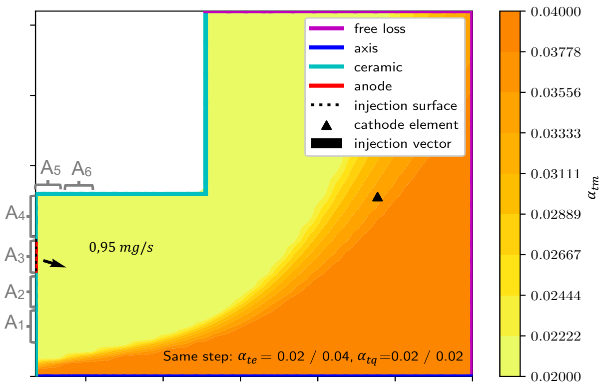

Figure 4: CHT simulation domain: the grey brackets A_1 to A_6 show the anode/injection locations compared. The contours show the turbulent transport coefficients for momentum and energy equations, for the heat flux it is uniform.

The plasma potential profile is strongly affected by the anode location. As one can see in fig. 5, the equipotential lines roughly match the magnetic streamlines. This results in a large radial component of the electric field that tends to concentrate the ions on the axis in the chamber (fig. 6 shows a large plasma density upstream on the axis) but allows them to diverge in the plume. As the anode is displaced away from the top-left corner (case A_4), the high potential region expands over a wider volume, increasing the axial component of the electric field. As a consequence, moving the anode towards the thruster axis (case A_1) reduces the beam divergence.

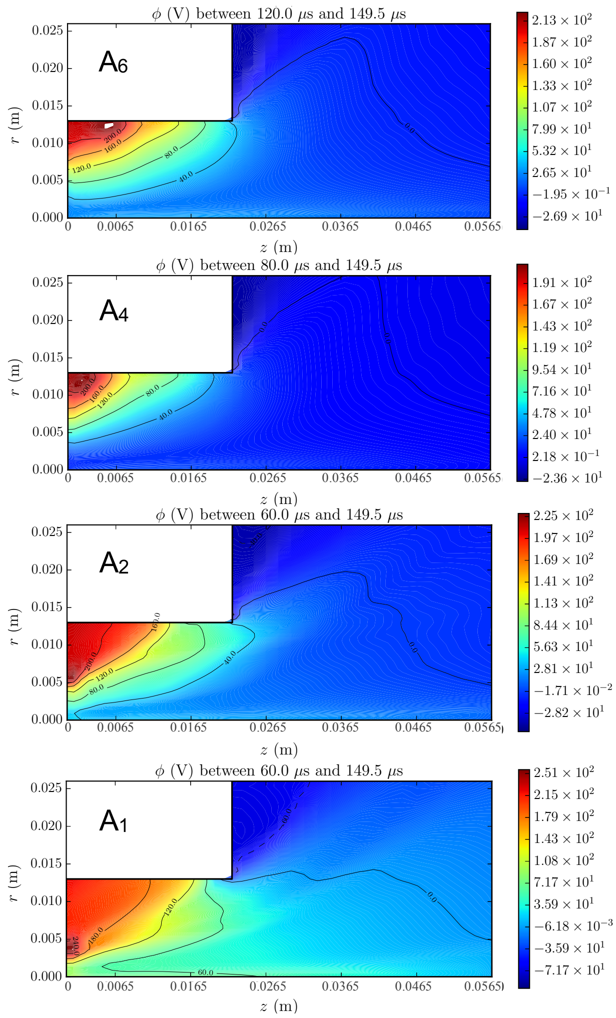

Figure 5: Electric plasma potential for anode locations A_1, A_2, A_4 and A_6.

In all cases, most of the ionization happens in the vicinity of the anode, since the neutrals are injected through it. Electrons are trapped along the magnetic field lines right downstream the anode, to which they eventually flow, and atoms must pass through this very collisional region. Another set of

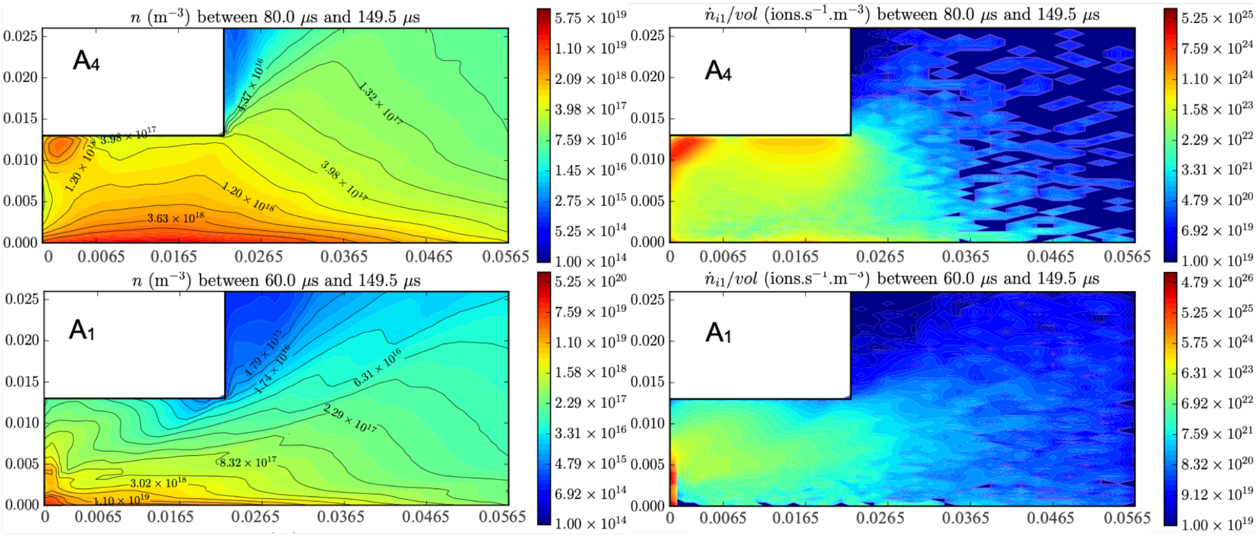

Figure 6: Comparison of plasma density (left) and ionization rate (right) for anode/injection positions A₁ and A₄.

simulations showed that good ionization or propellant utilization[3]

$$\eta_u = \frac{\dot{m}_{i\infty}}{\dot{m}_a} = \frac{I_{i\infty} M_i}{e\dot{m}_a}$$

can still be achieved separating anode and injector surfaces, if the former is further to the corner than the latter. The opposite configuration instead, results in neutrals leaking near the axis without any ionization. This brings some complementary information to [17] and [18] where anode and injection best locations were studied separately.

Fig. 6 highlights that having the anode near the corner -either on the back or sidewall- enhances the direct flow of ions to the downstream part of the sidewall. This was observed with ion current density stream plots: ions reach the ceramic wall, deposit their energy and recombine into neutrals, increasing the gas density n_n locally. These neutrals are re-ionized, which explains the greater plasma density and ion production near the sidewall and the channel exit plane, on the top plots of fig. 6. These multiple ionizations represent a waste of energy and yields heterogeneous beam particles velocities since those ions are produced downstream of the maximum potential. It seems that the effect on neutral density at sidewall is also observable in [14]. The two bottom plots show that such phenomenon is largely avoided when the anode is brought close to the axis. This large ion flux to the wall suggests that shortening or bevelling the wall could increase the thruster lifetime and improve performance to some extent by reducing power losses and erosion. An optimal channel geometry should be sought to combine the respective assets of the CHT and a wall-less thruster [19].

Regarding the anode location, fig. 7 shows that case A₂ works best in terms of thrust or anode efficiency, here defined as

$$\eta_{thr} = \frac{T^2}{2\dot{m}_a P_d},$$

ignoring cathode or coils power [7]. Sliding the anode away from the corner means that electrons cross fewer magnetic field lines to reach it. In case A₁, the electron current to the anode increases enough to reduce the current utilization efficiency $\eta_{cur} = \frac{I_{i\infty}}{I_d}$ beyond the gain in divergence efficiency $\eta_{div} = \frac{P_{zi\infty}}{P_{i\infty}}$ and voltage utilization η_{vol} (only estimated from the other efficiencies considering $\eta_{thr} = \eta_u \eta_{div} \eta_{cur} \eta_{vol}$). Note that this increase of I_e without large modification of I_i consequently raises the discharge current I_d and power P_d. To illustrate that the anode is shielded the most when in the corner, along with the current utilization provided in fig. 7, the discharge powers are the following $P_{d,A_1} = 495\ W$, $P_{d,A_2} = 418\ W$, $P_{d,A_4} = 293\ W$, $P_{d,A_5} = 285\ W$, $P_{d,A_6} = 400\ W$ (note that for A1, the power is still very high even though $\dot{m}_a$ is lower).

In cases A₅ and A₆, the anode is placed on the sidewall and behaves very similarly to case A₄. The smoother potential gradient created with the anode downstream (A₆) allows for better acceleration of all the ions produced, but just like in case A₁, the anode is more easily accessible for the electrons, because it is further away from the shielded corner, and the drop of η_{cur} annihilates most of the other benefits. Since the electric field near the back wall is almost purely radial (fig. 5A₆), some ions tend to backflow

[3] Indices i, ∞, a, z, d respectively refer to ion, at free-loss boundary (beam), anode, axial and discharge

to the wall near the axis, where the local energy flux becomes about four times greater than in case A_4.

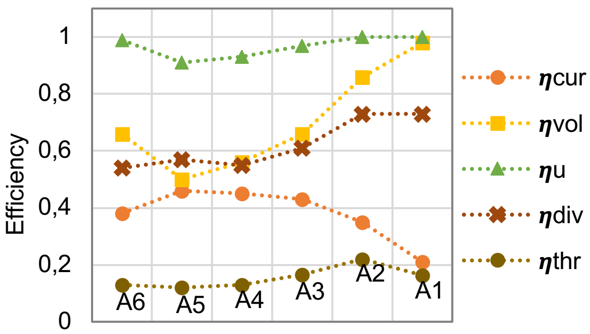

Figure 7: Partial and thrust efficiencies estimated for test cases A_1 to A_6.

3.3.2. Channel length and magnetic topology

Given the above observations on the thruster geometry, a study has been performed to compare three different channel lengths L_1, L_2 and L_3 as shown in fig. 8 while all the other parameters are kept constant. However, displacing the downstream edge of the thruster implies moving the front coil[4] more upstream, bringing it closer to the other coil. As a consequence, the magnetic field is slightly stronger and more radial when the channel is shortened (length L_1) as shown in fig. 9.

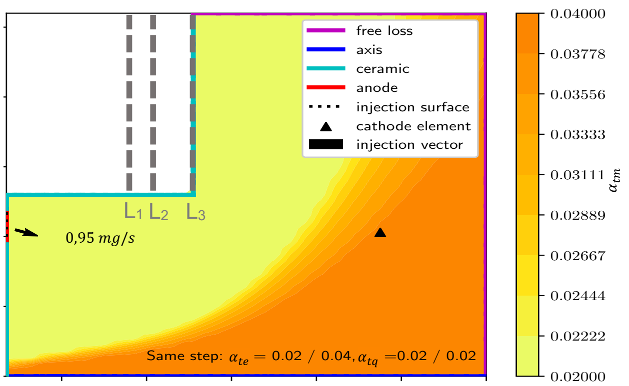

Figure 8: CHT simulation domain: the grey dashed lines indicate the channel lengths compared L_1, L_2 and L_3. The contours show the turbulent transport coefficients for momentum and energy equations, for the heat flux it is uniform.

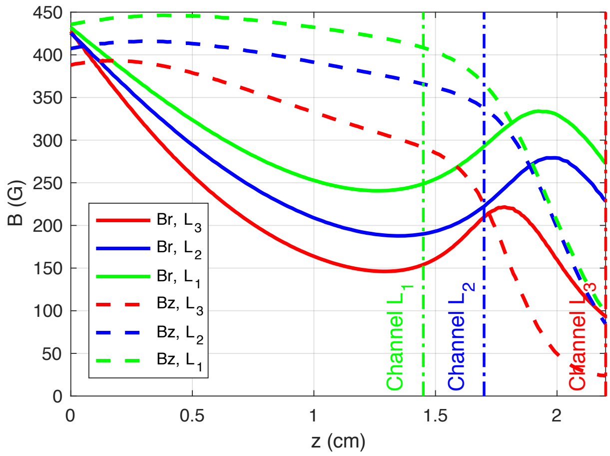

Figure 9: Modification of the axial and radial magnetic field (at the sidewall) for each channel length.

The main observation when using a shorter chamber is what motivated this study: the effective reduction of ions flowing to the sidewall at the channel exit and recombining into neutrals (that are ionized again), as fig. 11 shows. The energy deposited by ions on the sidewall is significantly decreased and since most ions are produced upstream in the channel and accelerated right away, the average velocity in the beam is larger. Fig. 10 shows the mean axial velocity of the ions along z at the quarter of the channel. The pit of the red line (length L_3) around $z = 1.5\ cm$ corresponds to the re-ionized neutrals from the sidewall mentioned above. The average velocity is decreased by these slow ions created downstream and accelerated by only a fraction of the total potential gradient. Cases L_1 and L_2 instead reach higher ion velocities since few ions are produced downstream in the channel. The green line (case L_1), however, displays a peak and a pit around $z = 3.4\ cm$ and $z = 2.1\ cm$ respectively, which are attributed to the magnetic streamline of the cathode crossing the plotted line. The electric field there seems to converge towards this $\vec{B}$ line and affects the axial and radial ion velocities (this effect is visible in fig. 13-top). Note that in fig. 10, it is visible that the ions are still being accelerated where the simulation domain ends, which supports that the performance magnitudes mentioned here can be underestimated due to the difficulty to place the free-loss boundary further downstream,

[4] Front coil refers to the outer-downstream one, while back coil refers to the inner-upstream one

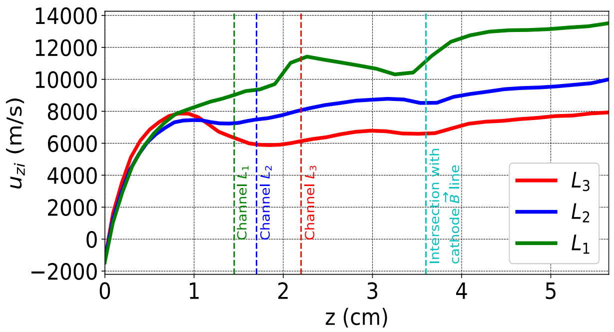

Figure 10: Single ion axial velocity along the axial direction, at 53% of the channel radius (see fig. 13), averaged in time and particles, for channel lengths L_1, L_2, L_3.

The discharge power in these three simulations is around 270W (±20W) and reducing the length enhances all the partial efficiencies. As a consequence, η_{thr} for cases L_1, L_2 and L_3, respectively, is 30%, 20.5% and 14.2%. To demonstrate that this improvement is due mainly to the channel geometry and not to the variation of $\vec{B}$ as presented in fig. 9, case L_3 was tested numerically with each of the three magnetic topologies, and no significant difference was observed ($\Delta\eta_{thr} < 0.4\%$). The above conclusions on the channel length effects are not in very good agreement with the experimental parametric studies carried out in [20] and [21], but the comparison is delicate given the numerous differences. Nevertheless, this suggests that the effect of varying the channel length depends on other elements such as the power level, the anode mass flow rate, the magnetic configuration (direct or cusped field) or the modification of $\vec{B}$ associated with the variation of either the length or the diameter. Those are the main differences identified between these studies.

Coupling the best results from sections **3.3.1.** and **3.3.2.** by placing the anode near the axis in a short thruster chamber does not allow for significant further improvement of the discharge properties, which could indicate that there is an ideal anode/injection location associated to each channel length.

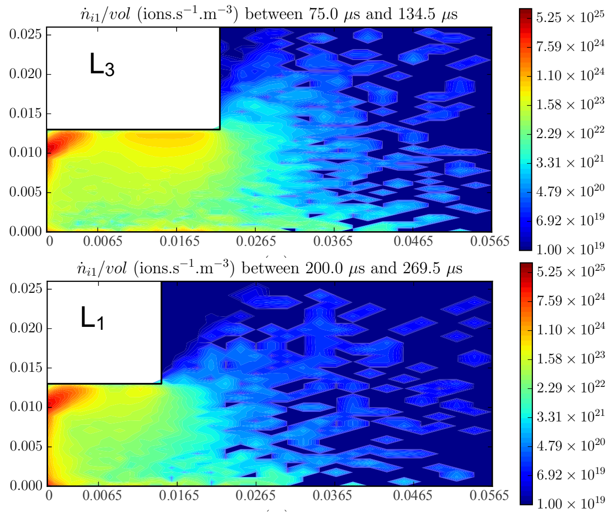

Figure 11: Ion production rate per unit volume for channel lengths L_1 and L_3, the colour scales are identical for comparison.

3.3.3. Cathode location

Case L_3 of section **3.3.2.** is used again to evaluate the effect of moving the cathode in the domain. Five positions are considered: C_1, C_2 and C_3 displace the cathode along the same magnetic isoline, while C_2, C_4 and C_5 displace it along the same magnetic streamline as pictured in fig. 12[5].

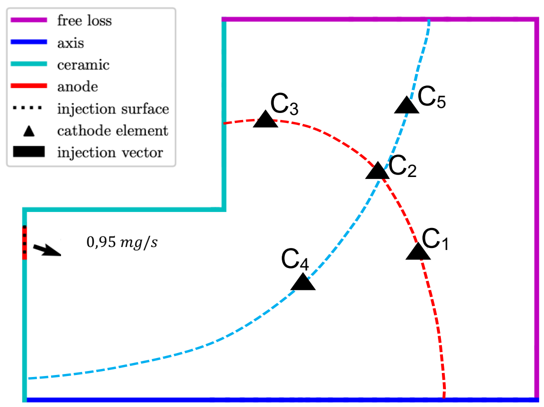

Figure 12: CHT simulation domain: the black triangles show the cathode positions tested in cases C_1 to C_5, the red and blue dashed lines represent a magnetic isoline and streamline, respectively.

When the cathode is placed on different magnetic streamlines (cases C_1, C_2, C_3), the electric field $\vec{E}$ in the plume is affected, mostly upstream the cathode streamline. Just beyond the channel exit plane, between cases C_1 and C_3, as shown in fig. 13, the radial component of $\vec{E}$ increases while its axial

[5] C_1, C_2 and C_4 are too much in the plasma beam to be achievable in reality with a hollow cathode, but can be with a filament cathode for research purposes

component is degraded, leading to a more divergent ion beam. However, since most of the accelerating potential occurs inside the chamber, this alteration of the electric field in the plume has a rather limited negative impact. Displacing the cathode on different isolines (cases C_2, C_4, C_5) does not seem to modify $\vec{E}$.

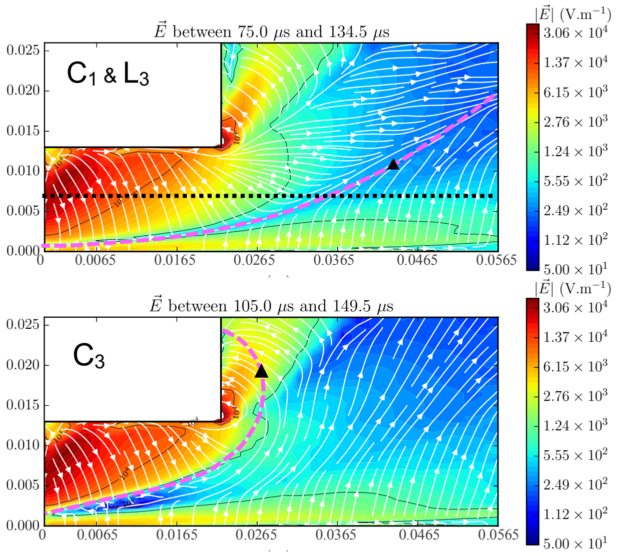

Figure 13: Direction and magnitude of the electric field in the CHT for cathode positions C_1 and C_3. The triangle is the cathode in C_1 (same as L_3), the dashed pink and black lines are the cathode $\vec{B}$ line and the quarter line (used in fig. 10)

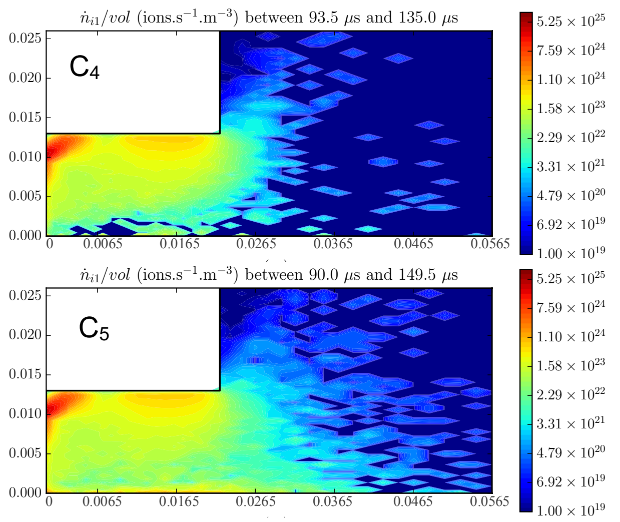

Figure 14: Ion production rate per unit volume for cathode positions C_4 and C_5 ($\dot{n}_i$ is very similar in cases C_1 and C_5), the colour scales are identical for comparison.

The cathode axial coordinate slightly affects the ionization region, which seems to expand from the anode down to this axial position, as presented in fig. 14. Even though these ions are not well accelerated, once again, the effect is very small because few of them are produced in the plume in comparison with the main ionization region, near the anode. Of all five simulations, the best results are offered by C_1 and C_4, where the cathode is the closest to the axis. In case C_1, many ions are produced, and the beam divergence is low, while in case C_4, the acceleration is improved by avoiding slow ions. Case C_3 has the least satisfying behaviour mainly because of the divergent electric field.

Besides, this study has evidenced the need to better understand the relation between the cathode location and turbulent transport. In particular, in case C_3, having the cathode magnetic streamline significantly *upstream* from the step in the profile of α_{tm} and α_{te} (defined in section **3.2.** and their step profile is showed in fig. 8) resulted in peculiar electron trajectories in between. This will not be further developed here since the profile selected for the anomalous transport coefficients is still rather arbitrary.

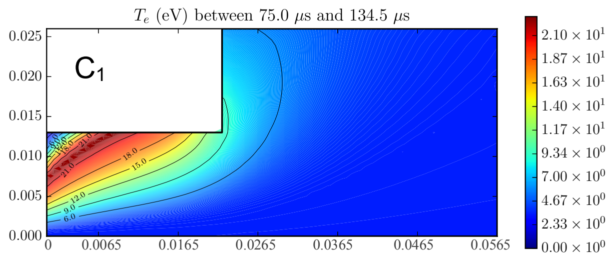

Figure 15: Electron temperature profile for case C_1.

In these five simulations, the discharge power set around $295W$ (±7W) and the electron temperature profile remained similar no matter the cathode location. T_e from case C_1 is presented in fig. 15 and is a quite typical result obtained with the simulations. Note that case C_1 provides a thrust $T = 8.9mN$ but operates at an unusually high discharge current $I_d \approx 1.5A$ compared to existing experimental results of CHT close to this power range [2]. This is due to the high anode mass flow rate which is chosen here to have a stable discharge with the selected anomalous contributions to electron transport. When experimental results of the prototype designed are available, these α_t parameters, among others, will be tuned to match the simulations with the tests. The electron and ion current densities of case C_1 can be visualized in fig. 16, top and bottom graphs respectively. The plot of $\vec{j}_e$ shows that the cathode magnetic field line carries most of the parallel electron current into the channel. In between the cathode and anode lines, inside the chamber, the electrons travel mostly azimuthally in an $\vec{E} \times \vec{B}$ drift and collisions allow them to transit across the $\vec{B}$ lines towards the anode.

In the plume, at the boundary, $\vec{j}_e$ balances the ion current.

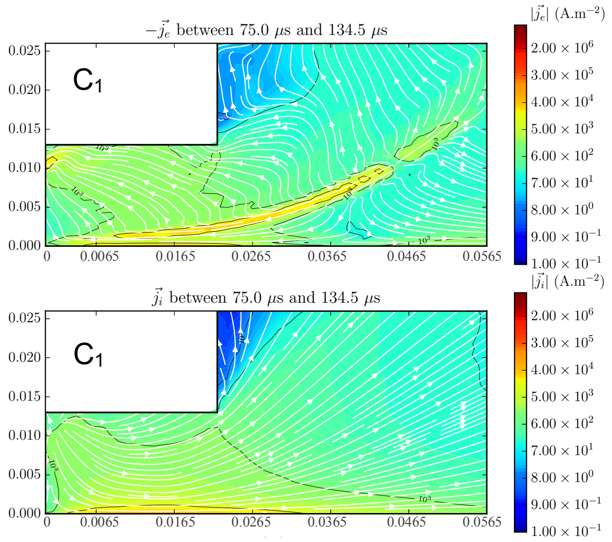

Figure 16: Time-averaged magnitude and streamlines of the electron (top) and ion (bottom) current densities in case C₁.

The bottom plot in fig. 16 shows that most of the ion current is carried along the thruster axis due to the focusing electric field inside the chamber, which is consistent with the typical large plasma density on the axis visible on fig. 6 (left)[6]. It also highlights the trajectory of ions flowing from the main ionization region to the sidewall, as mentioned in sections **3.3.1.** and **3.3.2.**, where they recombine into neutrals to be re-ionized. Finally, this fig. 16 shows some ion backflow to the back wall that results in energy deposition.

3.3.4. Thermalization factor

After studying the impact of various design options, this section focuses on understanding the effect of a physical phenomenon that is observed but not well quantified, namely the depletion of the high energy tail of the electron velocity distribution function (EVDF) by wall collection [22]. This could also eventually give design guidelines since thermalization is partially affected by secondary electron emission which depends on the channel wall material. The sheath model used in HYPHEN models the replenishment of the EVDF by including a thermalization coefficient σ_{th}, which is the ratio of the net flux of primary electrons to the wall versus a Maxwellian flux with the same temperature (considering reflected electrons). σ_{th} is used in the expression of the net flux of primary electrons to the wall, as:

$$g_p = \sigma_{th}(1-\delta_r)n_e\sqrt{\frac{T_e}{2\pi m_e}}e^{-\frac{e\Delta\Phi_{sh}}{T_e}},$$

with T_e, n_e at the sheath edge and δ_r the fraction of reflected primary electrons.

In this section, three values of thermalization factor are compared: $\sigma_{th} = 0.1$ then $\sigma_{th} = 0.3$ and $\sigma_{th} = 0.9$. Note that a value of 0.9 is not expected to be observable in reality since thermalization is limited by low collisionality. However, it could be interesting to assess the effect of the peculiar magnetic topology of the CHT with a large angle of the $\vec{B}$ lines at the wall. It is currently being investigated for traditional HET.

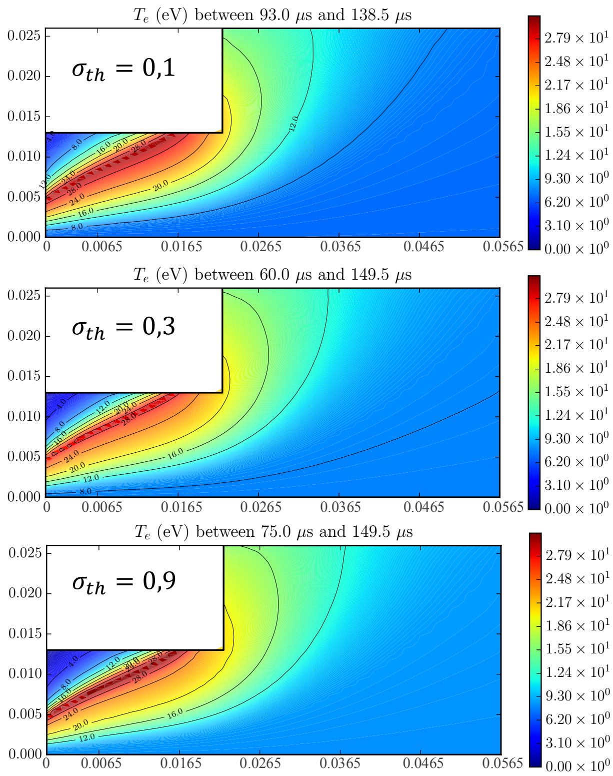

Figure 17: Electron temperature profile for the three thermalisation coefficients investigated (the colour scales are identical for comparison)

The results of these three simulations highlight that the most extreme cases (0.1 and 0.9) induce a slight increase of the maximum electron temperature in the plasma chamber, compared to $\sigma_{th} = 0.3$ (fig. 17, note that the anode is located in position A_2 from section **3.3.1.**). In the case of low thermalization, the average T_e is increased, probably due to the true

[6] This figure depicts results of another simulation but the large density on the axis is always observed

secondary electrons accelerated by the sheath (i.e. those emitted, not reflected, by electron impact with the wall). For very large thermalization, the replenished tail of the Maxwellian raises that average temperature. With medium thermalization fractions, these two phenomena balance each other and result in a lower T_e.

Lowering σ_{th} is seen to reduce $\Delta\Phi_{sh}$ and increase true secondary electron emission δ_{SEE} as presented in fig. 18-top along the sidewall and back wall. It is suggested that secondary electrons gain a significant amount of energy through the sheath, thus the non-thermalized secondary electrons can further induce SEE. This increases the electron density at the dielectric surface, lowering the wall potential which means electrons with lower energies can overcome the sheath barrier. On the top graph in fig. 18, one can see that for $\sigma_{th} = 0.1$, in the region of hot electrons[7], the sheath is saturated by large SEE, and $\Delta\Phi_{sh}$ almost vanishes. Note also that on fig. 18-top, the area of null SEE is the metallic anode where SEE is negligible.

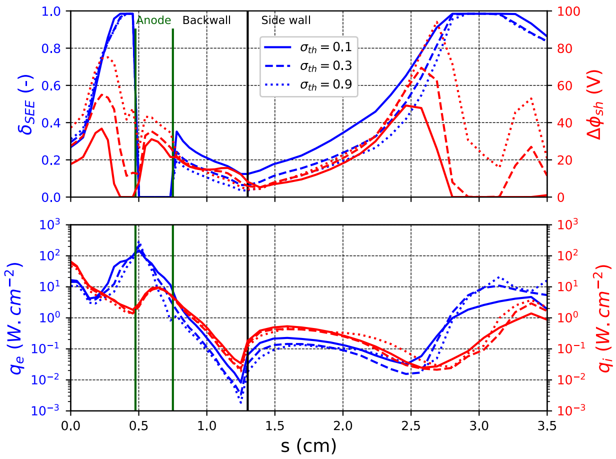

Figure 18: Secondary Electron Emission yield (blue) and sheath potential drop (red) (top) and energy flux to the wall from electrons (blue) and ions (red) (bottom), along back and sidewall starting from the axis, for three different thermalization coefficients (plain, dashed and dotted lines)

The consequence of decreasing σ_{th} is also visible on fig. 18-bottom where q_e and q_i, the electron and ion energy fluxes to the walls, are depicted. On the sidewall (left part of the graph), the energy fluxes are small and lightly affected by the thermalization factor, except at the exit, where electrons are hot, and some ions are accelerated towards the wall by the divergent electric field. In this region, the energy deposited by ions is reduced because $\Delta\Phi_{sh}$ is smaller, making the sheath less electron-confining. Regarding the electrons, q_e is reduced as well. The reason could be that even if slower electrons can overcome $\Delta\Phi_{sh}$, the tail is largely depleted so q_e does not rise significantly, but instead, secondary electrons are emitted by the wall at a chosen temperature (in this case $T_{se} = 2\,eV$) so the net energy flux at the wall is reduced for a small σ_{th}. This effect is probably quite sensitive to T_{se}.

On the back wall (fig. 18-bottom, right part of the graph), the electron energy flux to the anode is decreased when σ_{th} is decreased and the ion energy flux to the ceramic on the axis is increased. Those two regions receive energy fluxes substantially larger than elsewhere. The important reduction of power losses to the walls ($30\,W \cdot cm^{-2}$ less with $\sigma_{th} = 0.1$ than with $\sigma_{th} = 0.9$) results in more power used in ionizing collisions. The plasma potential in the channel is more axial and the plasma density on the axis is slightly higher. Those variations positively affect all the partial and thrust efficiencies. The aforementioned increase of ion energy flux to the wall at the axis is probably due to the greater number of ions produced: the density is larger on the axis and as specified earlier, $\vec{E}$ tends to accelerate some of the ions towards the wall in this region. This thermalization parameter now requires experimental results for comparison and matching, to provide better understanding of the electron energy distribution function in the discharge.

4. CONCLUSIONS

The design of a 200W CHT prototype was briefly introduced including choices of geometry and materials. The very first tests provided some promising observations, but further work is necessary to understand how to operate the thruster satisfyingly and start characterizing its plume. Then, the CHT has been studied numerically using the HYPHEN PIC/fluid simulation tool. The effect on the plasma discharge of the anode and injector location has been investigated and showed the existence of an optimal radial anode position on the back wall for a fixed channel geometry. This location allows for combining the maximum shielding of the electrode when it is placed in the corner, and the reduced ion energy deposition and recombination to the sidewall when it is placed near the axis. Then, the channel length was progressively reduced, which appeared to significantly enhance the thruster performance by avoiding ion flow to the sidewall near the exit plane. The short channel geometry thus reduces energy deposition to the wall, ions recombination into

[7] $r \sim 0.0045\,m$ on the back wall and $z \sim 0.0165\,m$ on the sidewall, in fig. 17, which corresponds to $s \sim 0.45\,cm$ and $s \sim 3\,cm$ in fig. 18

neutrals, and re-ionization of those neutrals. Finally, the cathode has been displaced in the plume to show that having it near the axis helps to narrow the beam angle. It also showed that a cathode placed upstream in the plume results in a more local ion production region, so a more uniform acceleration, but a smaller quantity of ions created. Eventually, changing the thermalization coefficient for the plasma electrons demonstrated that a low thermalization reduces the sheath potential, increases the secondary electron emission and globally decreases power losses to the walls sufficiently to enhance the thruster's performance. Measurements are now needed to compare with these observations on thermalization and deduce what is a realistic value.

5. ACKNOWLEDGEMENTS

This work has been supported by the Projects PID2019-108034RB-I00/AEI/10.13039/501100011033 (Spain's National Research and Development Plan) and ESP2016-75887 (Spain's National Research and Development Plan - MINECO/ FEDER).

6. REFERENCES

1. Ahedo, E. & Gallardo, J. M. (2003). Scaling down Hall thrusters. in *28th International Electric Propulsion Conference*.
2. Smirnov, A., Raitses, Y. & Fisch, N. J. (2006). Experimental and theoretical studies of cylindrical Hall thrusters. *Physics of Plasmas* **14**, 057106.
3. Kim, H., Lim, Y., Choe, W. & Seon, J. (2014). Effect of multiply charged ions on the performance and beam characteristics in annular and cylindrical type Hall thruster plasmas. *Appl. Phys. Lett.* **105**, 144104.
4. Gao, Y., Liu, H., Hu, P., Huang, H. & Yu, D. (2016). The effect of magnetic field near the anode on cylindrical Hall thruster. *Plasma Sources Sci. Technol.* **25**, 035011.
5. Brieda, L. & Keidar, M. (2011). Multiscale Modeling of Hall Thrusters. in 13.
6. Shirasaki, A. & Tahara, H. (2007). Operational characteristics and plasma measurements in cylindrical Hall thrusters. *Journal of Applied Physics* **101**, 073307.
7. Dominguez-Vazquez, A., Zhou, J., Fajardo, P. & Ahedo, E. (2019). Analysis of the plasma discharge in a Hall thruster via a hybrid 2D code. in *36th International Electric Propulsion Conference*.
8. Jiang, Y., Tang, H., Ren, J., Li, M. & Cao, J. (2018). Magnetic mirror effect in a cylindrical Hall thruster. *J. Phys. D: Appl. Phys.* **51**, 035201.
9. Ikeda, T., Togawa, K., Tahara, H. & Watanabe, Y. (2013). Performance characteristics of very low power cylindrical Hall thrusters for the nano-satellite "PROITERES-3". *Vacuum* **88**, 63–69.
10. Raitses, Y., Merino, E. & Fisch, N. J. (2010). Cylindrical Hall thrusters with permanent magnets. *J. Appl. Phys.* 10.
11. Kim, H., Choe, W., Lim, Y., Lee, S. & Park, S. (2017). Magnetic field configurations on thruster performance in accordance with ion beam characteristics in cylindrical Hall thruster plasmas. *Appl. Phys. Lett.* **110**, 114101.
12. Raitses, Y., Smirnov, A., Granstedt, E. & Fisch, N. (American Institute of Aeronautics and Astronautics, 2007). Optimization of Cylindrical Hall Thrusters. in *43rd AIAA/ASME/SAE/ASEE Joint Propulsion Conference & Exhibit*.
13. Smirnov, A., Raitses, Y. & Fisch, N. J. (2003). Enhanced ionization in the cylindrical Hall thruster. *Journal of Applied Physics* **94**, 852–857.
14. Garrigues, L. *et al.* (2008). Simulations of a Miniaturized Cylindrical Hall Thruster. *IEEE Trans. Plasma Sci.* **36**, 2034–2042.
15. Matyash, K., Schneider, R., Kalentev, O., Raitses, Y. & Fisch, N. J. (2011). Numerical investigations of a cylindrical Hall thruster. in *The 32nd International Electric Propulsion Conference*.
16. Brieda, L. & Keidar, M. (2013). Multiscale Modeling of Hall Thrusters. in *33rd International Electric Propulsion Conference* 13.
17. Gao, Y., Liu, H., Hu, P., Huang, H. & Yu, D. (2017). Effect of anode position on the performance characteristics of a low-power cylindrical Hall thruster. *Physics of Plasmas* **24**, 063518.
18. Gao, Y., Liu, H., Hu, P., Huang, H. & Yu, D. (2016). Performance characteristics according to the radial position of gas distributor holes in a low-power cylindrical Hall thruster. *Physics of Plasmas* **23**, 083514.
19. Simmonds, J. & Raitses, Y. (2019). Miniaturized Cylindrical Hall Thrusters: Magneto-Electrostatic Trap Thruster. in *the 36th International Electric Propulsion Conference*.
20. Lee, J., Seo, M., Seon, J., June Lee, H. & Choe, W. (2011). Performance characteristics according to the channel length and magnetic fields of cylindrical Hall thrusters. *Appl. Phys. Lett.* **99**, 131505.
21. Seo, M., Lee, J., Seon, J., June Lee, H. & Choe, W. (2013). Radial scale effect on the performance of low-power cylindrical Hall plasma thrusters. *Appl. Phys. Lett.* **103**, 133501.
22. Ahedo, E., De Pablo, V. & Martinez-Sanchez, M. (2005). Effects of partial thermalization and secondary emission on the electron distribution function in Hall thrusters. in *29th International Electric Propulsion Conference* 11.